Copper(I) Iodide as Hole-Conductor in Planar Perovskite Solar Cells: Probing the Origin of *J–V* Hysteresis

*Gaveshana A. Sepalage, Steffen Meyer, Alexander Pascoe, Andrew D. Scully, Fuzhi Huang, Udo Bach, Yi-Bing Cheng, and Leone Spiccia**

Organic–inorganic lead halide perovskite solar cells are promising alternatives to silicon-based cells due to their low material costs and high photovoltaic performance. In this work, thin continuous perovskite films are combined with copper(I) iodide (CuI) as inorganic hole-conducting material to form a planar device architecture. A maximum conversion efficiency of 7.5% with an average efficiency of 5.8 ± 0.8% is achieved which, to our knowledge, is the highest reported efficiency for CuI-based devices with a planar structure. In contrast to related planar 2,2′,7,7′-tetrakis-(*N*,*N* -di-4-methoxyphenylamino)-9,9′-spirobifluorene (spiro-OMeTAD)-based devices, the CuI-based devices do not show a pronounced hysteresis when tested by scanning the potential in a forward and backward direction. The strong quenching of photoluminescence (PL) signal and comparatively fast decay of open-circuit voltage demonstrates a more rapid removal of positive charge carriers from the perovskite layer when in contact with CuI compared to spiro-OMeTAD. A slow response on a timescale of 10–100 s is observed for the spiro-OMeTAD-based devices. In comparison, the CuI-based device displays a significantly faster response as determined through electrochemical impedance spectroscopy (EIS) and open-circuit voltage decays (OCVDs). The characteristically slow kinetics measured through EIS and OCVD are linked directly to the current–voltage hysteresis.

1. Introduction

Hybrid organic–inorganic perovskite solar cells are attracting significant interest as a result of the rapid increase in record power conversion efficiencies (PCEs) from 3.6% to values currently exceeding 20% within a few years.[1–7] For the majority of these devices, two configurations of the photoactive layer have been employed: (i) a mesoporous-structured layer in which the photoactive organo lead iodide perovskite ($APbI_3$) is infiltrated into the mesoporous material,[8] or (ii) a thinner dense planar-structured $APbI_3$ film,[9,10] where A is an organic cation, typically alkylammonium[5] or formamidinium,[11,12] usually deposited onto an electron-extracting layer. Both the mesoporous and planar films have produced high device efficiencies when effective electron-transporting and hole-transporting materials (HTMs) have been utilized.[13–17] Titanium dioxide has been used widely as an efficient and stable electron-extracting layer, although other materials such as ZnO[18] or [6,6]-phenyl-C_{61}-butyric acid methyl ester (PCBM)[19,20] have also resulted in devices with high performance, whereas devices without an electron-extracting layer have been reported with up to 14% efficiency.[21] A different structure in which the hole-conductive layer is deposited directly onto the substrate followed by the perovskite layer and electron-conductive material on the top of the HTM, usually referred to as “inverted” in the perovskite solar cell field, has also been reported.[20,22,23]

In the first reports of perovskite solar cells, liquid-state electrolytes based on I^-/I_3^- redox couple were employed, which resulted in inferior performance.[1,24] In contrast, the application of solid-state organic HTMs, such as 2,2′,7,7′-tetrakis-(*N,N*-di-4-methoxyphenylamino)-9,9′-spirobifluorene (spiro-OMeTAD),[8,25] poly(triarylamine) (PTAA),[7,16] and poly(3-hexylthiophene) (P3HT)[26] in perovskite solar cells has resulted in outstanding device efficiencies. Perovskite-based devices largely derive their origins from dye-sensitized solar cells (DSSCs). In DSSCs, the mesoporous n-type semiconductor and adjacent HTM separate the electrons and holes generated by the light absorption of the dye.[27] In this regard, the aforementioned HTMs served as charge-separating materials as well as hole-conducting materials. Perovskite-based cells are characterized by the rapid dissociation of excitons within the perovskite layer,[28] and free carriers are generated within the light-absorbing material itself.[31] Due to this distinction, the design of HTMs for high efficiency perovskite-based devices differs from that for DSSCs, despite the fact that both technologies have a common history.

G. A. Sepalage, Dr. S. Meyer, Prof. L. Spiccia
School of Chemistry
Monash University
Victoria 3800, Australia
E-mail: leone.spiccia@monash.edu

A. Pascoe, Dr. F. Huang, Prof. U. Bach, Prof. Y.-B. Cheng
Department of Materials Science and Engineering
Monash University
Victoria 3800, Australia

Dr. A. D. Scully, Prof. U. Bach
CSIRO Manufacturing Flagship
Bayview Avenue, Clayton, 3168 Victoria, Australia

Prof. U. Bach
Tech Fellow, The Melbourne Centre for Nanofabrication
151 Wellington Road, Clayton, 3168 Victoria, Australia

DOI: 10.1002/adfm.201502541

The organic HTMs are typically doped with lithium bis(trifluoromethanesulfonyl)imide (LiTFSI) and 4-*tert*-butylpyridine (*t*-BP) with the aim of improving the device performance.[32–34] Although most high-efficiency perovskite solar cells generally employ organic hole conductors, they appear unlikely to feature in the commercialization of perovskite solar cells due to their cost (e.g., for spiro-OMeTAD) and uncertainties about long-term device stability. As device instability mainly results from the degradation of perovskite by oxygen and moisture,[35,36] the presence of a hygroscopic lithium salt in many organic HTMs is unfavorable.[37] Additionally, the other common additive, *t*-BP, has been reported to interact with the perovskite material,[38] and organic polymers with π-conjugated systems can be degraded by the presence of oxygen and light.[39] Therefore, one of the current challenges in perovskite solar cell research is either to design a stable HTM-free device or to find a suitable, low cost, and stable HTM.

Inorganic HTMs are promising alternatives to organic HTMs,[40,41] as are device structures that do not incorporate an HTM layer.[42,43] CuI,[41] CuSCN,[40,44–46] and NiO[47,48] have been successfully applied as inorganic HTMs and have led to maximum PCEs of 6.0%, 16.6%, and 14.9%, respectively. The meso-structured devices incorporated thick CuI or CuSCN HTM layers, each about 1 µm, deposited by solution-processed techniques on a mesoporous TiO_2/perovskite structure.[40,41] In comparison, the normal (i.e., non-"inverted") planar devices utilized a thinner perovskite film (≈500 nm), and efficiencies up to 7.2% were reported for devices using CuSCN as the HTM.[44,45] Although the perovskite film is more susceptible to being damaged by polar solvents during the inorganic HTM deposition process, the planar device architecture is highly attractive for future solar cell fabrication as it does not require sintering of a mesoporous scaffold.[17,18]

The current–voltage (J–V) hysteresis behavior of perovskite solar cells has been discussed widely in recent literature.[49–53] The current response of the reverse scan from open-circuit to short-circuit ($V_{oc} \rightarrow V_0$) generally produces higher currents compared to the forward scan from short-circuit to open-circuit ($V_0 \rightarrow V_{oc}$). Defects that act as electron traps in the perovskite film, conceivable ferroelectric properties of perovskite material, and ion migration have all been proposed as possible explanations for the hysteretic behavior.[49,54] Kim and Park[51] reported a reduction in the hysteretic behavior on introduction of a thick mesoporous titania film and ascribed this to fast charge extraction by the TiO_2 scaffold. Electrochemical impedance spectroscopy (EIS) measurements indicated a decrease in the low-frequency capacitance with the inclusion of a thick TiO_2 layer. In other studies, a slow response in transient measurements was attributed to the migration and accumulation of mobile ions at relevant selective contacts.[53,55] However, despite much research interest, the physical origins of the hysteresis are yet to be fully described.

The present study investigates the application of a solution-processed inorganic HTM (CuI) layer in planar-structured perovskite solar cells. The challenges addressed in this investigation include: (i) how to avoid the dissolution of perovskite film during inorganic HTM deposition; (ii) how to control the inorganic HTM morphology; and (iii) how to achieve good interfacial layer contacts. CuI was chosen as the inorganic HTM due to its higher solubility in organic solvents compared to CuSCN, and its higher hole mobility (CuI: 0.5–2 $cm^2\ V^{-1}\ s^{-1}$ vs. CuSCN: 0.01–0.1 $cm^2\ V^{-1}\ s^{-1}$).[56,57] To the best of our knowledge, there is only one reported application of CuI as an inorganic HTM in a perovskite solar cell. Kamat and co-workers[41] achieved a maximum PCE of 6.0% and average PCE of 3.7% for a cell-design consisting of a dense TiO_2 layer/meso-structured perovskite/CuI/gold. In the present work, an inorganic HTM has been successfully applied in planar-structured devices consisting of a dense TiO_2 layer/planar perovskite/CuI/graphite, and significant improvements in device performance were achieved. The CuI-based devices also displayed a greatly reduced current–voltage hysteresis compared to the conventional spiro-OMeTAD-based devices. The physical differences between these two HTMs, including the differences in the hysteretic behavior, were explored using time-resolved photoluminescence (PL) spectroscopy, EIS, and open-circuit voltage decay (OCVD) characterization techniques.

2. Results and Discussion

2.1. Device Fabrication and Optimization

In the first step of device assembly, a dense TiO_2 layer (≈50 nm) was deposited by spray pyrolysis of a $Ti(acac)_2({}^iPrO)_2$ solution on fluorine-doped tin oxide (FTO)-coated glass substrate. This dense layer acted as a hole-blocking layer and avoided contact between the HTM and the underlying FTO layer. As the $(CH_3NH_3)PbI_3$ perovskite layer used for planar device architecture is relatively thin, CuI can easily form short-circuits between the electrode and counter electrode through pinholes in the perovskite layer. Therefore, the coverage and thickness uniformity of the TiO_2 blocking layer were important to obtain reproducible devices with high performance.

The perovskite layer was deposited using a gas-assisted technique from a solution containing lead iodide and methylammonium iodide in DMF, as reported by our group recently.[58] This technique enables the formation of perovskite grains that are firmly adhered to the blocking layer and uniformly packed.[58] The perovskite film thickness was optimized for the CuI-based devices by varying the $(CH_3NH_3)PbI_3$ content in the precursor solution between 40 and 50 wt%, and applying a constant spin speed during film deposition (Figure S1, Supporting Information). The optimum was found to be 45 wt% leading to a perovskite layer thickness of 300–400 nm, which was also found previously to efficiently absorb sunlight in spiro-OMeTAD-based devices.[58]

The CuI layer was deposited by doctor blading a solution of CuI in di-*n*-propylsulfide/chlorobenzene solvent mixture under ambient conditions, as described in the methods section and reported previously by Christians et al.[41] To fabricate the CuI film, it was important to move the hand-driven drawdown bar (**Figure 1**a) rapidly to ensure that the di-*n*-propylsulfide (Pr_2S) solvent evaporates quickly and does not interact with the underlying perovskite layer. The arrangement of the perovskite and CuI layers are clearly visible in the scanning electron microscopy (SEM) images (**Figure 2**a,b). The images show that there is a distinct separation between each layer. The CuI

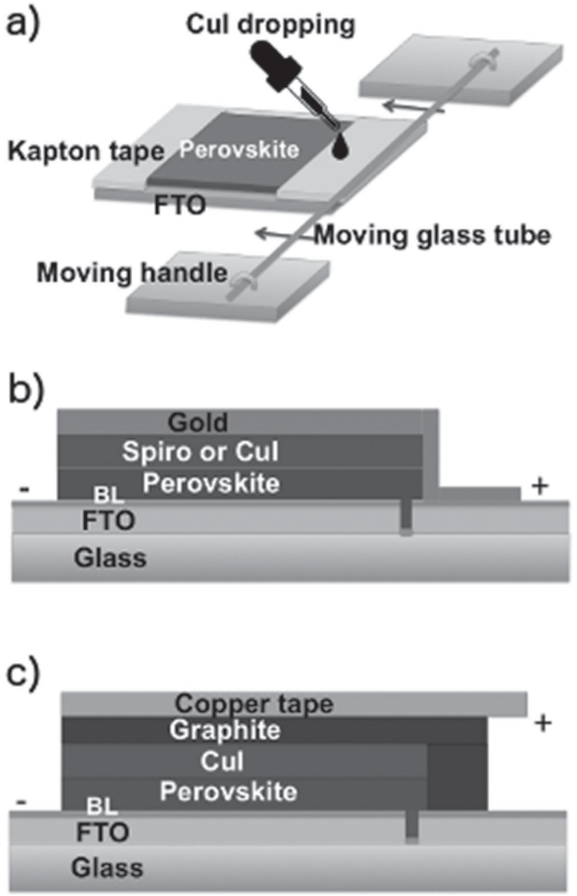

Figure 1. Schematic drawings (not to scale) of a) CuI deposition by manual doctor blading and architectures of devices constructed with: b) gold; c) graphite counter electrodes.

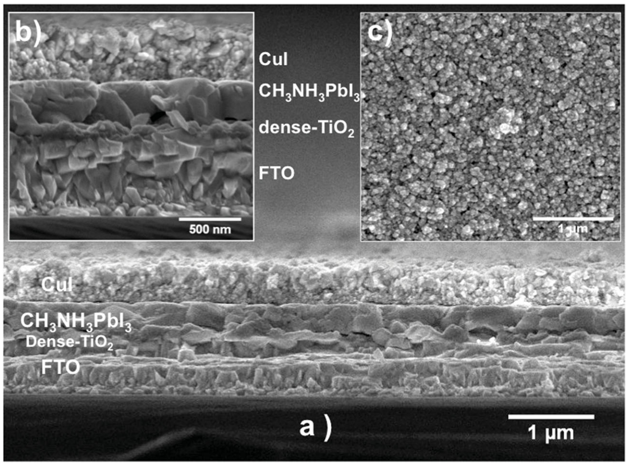

Figure 2. SEM images of a perovskite solar cell with CuI as HTM: a) cross section; b) cross section at higher resolution; and c) top view of the CuI surface. The devices were not coated with graphite for the cross-sectional SEM images to obtain a clearer image and avoid graphite particles covering the cross section.

layer used in this study was approximately 400 nm thick and consisted of small particles that are connected to form a 3D structure (Figure 2b,c). The CuI surface was found to be rough and showed gaps between particles (Figure 2c). No systematic variation in device performance was found as a function of the CuI film thicknesses, which ranged from <200 nm to 1 µm (Figure S2, Supporting Information). An alternative method involving spin coating of an equivalent solution was also trialed, but did not produce a uniform CuI film. Therefore, the doctor-blading method was employed in device fabrication.

Kamat and co-workers have reported mesoporous structured CuI-based devices comprising a gold counter-electrode.[41] In the present study, planar-structured devices were fabricated using either a gold or graphite counter-electrode. Graphite layers fabricated using doctor blading resulted in devices with superior performance (**Figure 3**) than devices comprising a gold counter-electrode (Figure S4, Supporting Information). It is thought that the rough CuI surface and the presence of gaps between particles in the planar structure increase the possibility of forming short-circuits upon deposition of gold. In contrast, for the spiro-OMeTAD-based devices, the performance was significantly increased using a gold counter electrode (Figure 3) compared to the graphite counter electrode (Figure S6, Supporting Information). For the latter, solvent-based graphite deposition was less successful because the spiro-OMeTAD layer dissolved in the chlorobenzene present in the graphite dispersion. As an alternative method, a pressed graphite layer was transferred on the top of the organic HTM in this study. A comprehensive overview of the various device-type performances as a function of counter-electrode materials is presented in Table S1 (Supporting Information). Based on these results, a gold counter-electrode was used for spiro-OMeTAD-based devices and a graphite counter-electrode for CuI-based devices in order to achieve optimum device performances.

2.2. Device Characterization

2.2.1. Photovoltaic Performance

The photovoltaic performance of a batch of 38 perovskite/CuI/graphite devices is shown in Figure 3a, and the distribution of the *J*–*V* parameters can be found in Figure S3 (Supporting Information). These data were obtained by reverse ($V_{oc} \rightarrow V_0$) scanning at 0.1 V s^{-1} rate. On average, the CuI-based devices achieved a short-circuit current density (J_{sc}) of 16.7 ± 1.0 mA cm^{-2}, an open-circuit voltage (V_{oc}) of 672 ± 80 mV, a fill factor (FF) of 0.52 ± 0.04, and an efficiency (η) of 5.8 ± 0.8%. The best-performing cell achieved an efficiency of 7.5% (**Table 1**). The *J*–*V* results of a batch of 15 spiro-OMeTAD-based devices made using the same conditions are also shown in Table 1. The highest recorded efficiency was 15.8%, with an average of 14.1 ± 1.0%. The planar architecture adopted in this study, in combination with a graphite counter electrode has resulted in both higher performance and reproducibility compared to previously reported meso-structured CuI-based devices.[41] During the optimization process, a device efficiency above 5% was measured regardless of the perovskite film composition. This indicates that comparatively high efficiencies can be maintained despite changes in the thickness or texture of the perovskite film (Figure S1, Supporting Information). The

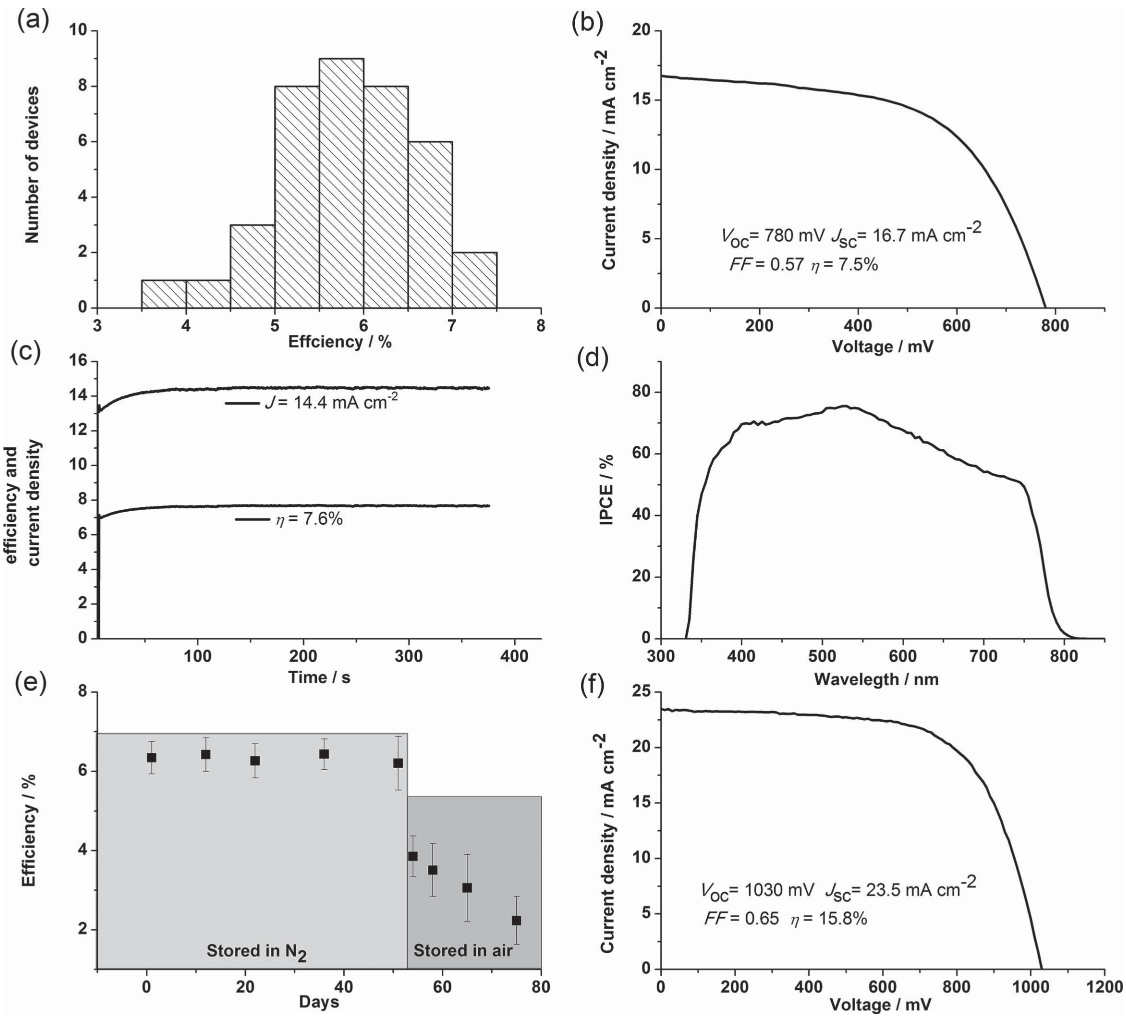

Figure 3. Characterization of planar-structured perovskite solar cells constructed with CuI as a HTM: a) PCE distribution for a batch of 38 devices; b) *J*–*V* curve of the best-performing FTO/TiO$_2$/perovskite/CuI/graphite device at 0.1 V s^{-1} scanning rate in reverse direction ($V_{oc} \rightarrow V_0$); c) steady-state current and efficiency of the best performing CuI-based device, measured at an applied bias of 530 mV; d) IPCE spectrum of the best performing CuI-based device; e) stability data of a batch of six CuI-based devices stored under nitrogen atmosphere and dark conditions for 50 d and afterwards in air for 25 d; f) *J*–*V* curve of the best performing FTO/TiO$_2$/perovskite/spiro-OMeTAD/gold device at 0.1 V s^{-1} scanning rate in reverse direction ($V_{oc} \rightarrow V_0$).

PCE also remained above 5% when the CuI layer thickness was varied between 75 and 1000 nm (Figure S2, Supporting Information).

For the best-performing CuI-based device, a steady-state efficiency of 7.6% was measured at an applied bias of 530 mV corresponding to the maximum power output (Figure 3c). The incident photon-to-current efficiency (IPCE) curve (Figure 3d) shows that the devices effectively harvest light across the entire visible spectral region, as has been documented previously for perovskite solar cells.[17,59–62] The integrated current density of 16.2 mA cm^{-2} calculated from the IPCE data is in good agreement with the J_{sc} value of 16.7 mA cm^{-2} measured for the best performing device. For comparison, the *J*–*V* performance of the best spiro-OMeTAD-based device is shown in Figure 3f.

Theoretically, the CuI-based perovskite solar cells should produce a V_{oc} of close to 1 V (cf. TiO$_2$ conduction band minimum at 4.2 eV, CuI valence band maximum at 5.2 eV).[5] However, our devices only achieved a V_{oc} of 672 ± 80 mV, although this is still higher than the 550 mV previously reported for meso-structured perovskite devices using CuI as an inorganic HTM.[41] This lower-than-expected voltage has been attributed to rapid recombination at the perovskite/CuI interface based on the high hole-mobility of CuI (0.5–2 cm^2 V^{-1} s^{-1})[56] compared to spiro-OMeTAD (1.6×10^{-3} cm^2 V^{-1} s^{-1}).[32] The average V_{oc} and average J_{sc} values in this study were significantly higher than CuI-based meso-structured devices[41] but the fill factors (FFs) were lower.

The improved V_{oc} and J_{sc} of the new CuI-based device architecture are postulated to arise from reduced interfacial electron-hole recombination and short-circuiting,[63] and to the improved reproducibility of the device performance. It is also possible that the rapid deposition of the thin HTM layer used in this study minimizes artifacts generated in perovskite layer, as discussed above. Additionally, a better CuI/counter electrode contact has been achieved employing graphite compared to gold, as evident from the performance of either device type;

Table 1. Comparison of the photovoltaic performance of planar devices based on CuI and on spiro-OMeTAD HTMs.

HTM/electrode	Statistic	J_{sc} [mA cm^{-2}]	V_{oc} [mV]	FF	η [%]
CuI/graphite	Best	16.7	780	0.57	7.5
CuI/graphite	Average	16.7 ± 1.0	672 ± 80	0.52 ± 0.04	5.8 ± 0.8
spiro-OMeTAD /gold	Best	23.5	1030	0.655	15.8
spiro-OMeTAD/gold	Average	21.2 ± 1.1	1030 ± 30	0.65 ± 0.03	14.1 ± 1.0

see Figure 3b (CuI/graphite) vs Figure S4 (Supporting Information) (CuI/gold). According to the latter *J–V* curve, CuI-based devices with a gold counter electrode are strongly shunted, indicating that gold penetrates into the nanostructured CuI during the thermal evaporation process. Despite the increased performance of CuI/graphite-based devices and excellent charge transport properties of CuI, these solar cells did not reach the high short-circuit currents exhibited by the spiro-OMeTAD-based devices. This reduction in the current can be attributed, in part, to the higher series resistance of the graphite electrode, as seen in the comparison between the spiro-OMeTAD/graphite and spiro-OMeTAD/gold devices (Table S1, Supporting Information, Figure 3f, Figure S6, Supporting Information). The average J_{sc} of CuI/graphite (J_{sc} = 16.7 mA cm^2) is reduced by approximately 20% compared to the high performing spiro-OMeTAD/gold devices (J_{sc} = 21.2 mA cm^{-2}). Another factor that leads to a decreased photocurrent is faster interfacial recombination at perovskite/CuI interface, as observed in the OCVD measurements (see below) and previously reported by Kamat and co-workers for meso-structured CuI-based devices.[41] The low V_{oc} observed in CuI-based devices as discussed above and the low recombination resistance shown by EIS measurements (see below) further confirm the faster rate of recombination. If recombination is fast enough to compete with charge extraction at short circuit, the short-circuit current (J_{sc}) will be reduced.

2.2.2. Stability

The stability of a batch of six non-sealed devices was recorded over a period of 50 d of storage under nitrogen in the dark (Figure 3e). These cells were exposed to air for ca. 1 h during each *J–V* characterization measurement before being returned to the nitrogen enclosure. The average PCE for these cells remained constant throughout the 50 d, indicating little degradation of the devices. After 50 d, the same devices were exposed to air for a further 25 d. The device performance declined rapidly, most likely due to the degradation of perovskite layer. It has been reported previously that moisture is capable of decomposing the perovskite material, leading to the formation of yellow-colored PbI_2 precipitate.[64,65] In comparison, meso-structured perovskite/CuI/Au devices have been exposed to air over a period of 54 d with little variation of device performance.[41] This implies that CuI HTM layer itself is suitably stable in air. The porosity of the graphite layer, coupled with a thinner CuI layer, used in the present work means that the devices are more susceptible to moisture ingress and subsequent degradation of the perovskite layer. Therefore, encapsulation of the active area is required for the sustained operation of the planar devices.

2.2.3. J–V Dependence on Scan Rate

Given the well-documented "hysteretic" behavior of normal (i.e., non-"inverted") planar-structured perovskite solar cells, the performance of the optimized CuI-based and spiro-OMeTAD-based devices was measured at a range of scan speeds in both forward ($V_0 \rightarrow V_{oc}$) and reverse ($V_{oc} \rightarrow V_0$) directions (**Figure 4**). Scans at 0.1, 1, and 0.04 V s^{-1} for CuI-based devices (Figure 4a–c, respectively) and spiro-OMeTAD-based devices (Figure 4d,e, respectively) illustrate the relatively minor hysteresis observed in the CuI-based device at all scan rates; the results are independent of scan rate, within experimental uncertainty. In contrast, the spiro-OMeTAD-based device displays a strong hysteresis at higher scan rates, which is reduced at lower scan rates. As an example, there were significant differences in the *J–V* curves for the spiro-OMeTAD-based devices at scan rate 0.1 V s^{-1}. Efficiencies of 10.3% and 14.3% were recorded in the forward and reverse directions, respectively. In comparison, the CuI-based device showed efficiencies of 7.6% and 7.5% in the forward and reverse directions, respectively.

2.2.4. Steady-State Current Measurements

In a typical *J–V* measurement, the current is recorded within a short time (10–250 ms, respective to scan rates of 1 to 0.04 V s^{-1}) after the bias is applied and there is little time for the systems to stabilize. The capacitive current that is stored or released by the perovskite material is too large to be corrected for this type of fast scans.[66] This capacitive current can result in a difference in the photocurrent measured during the forward and reverse scans leading to *J–V* hysteresis. We measured the steady-state currents of the devices with a 20 s settling time at each applied potential. The potential sweeps were performed in both forward and reverse directions. The results are shown in **Figure 5**. Spiro-OMeTAD-based devices typically took more than 20 s to deliver a stable current regardless of the scan direction (see Figure 5a,b). In contrast, the CuI-based devices displayed a much quicker response following each voltage step and the current typically stabilized after 1 s, as is clearly shown in Figure 5c,d. The faster response is suggestive of a lower capacitive current and, consequently, less hysteresis when CuI is used as the hole-conductor.

The results described so far pertain to *J–V* measurements carried out on spiro-OMeTAD-based devices comprising a gold counter-electrode and CuI-based devices comprising a graphite counter-electrode. To ensure that the hysteresis observed for the spiro-OMeTAD-based devices is unaffected by the counter-electrode material, *J–V* measurements were conducted on spiro-OMeTAD-based devices having a graphite counter-electrodes (FTO/dense-TiO_2/$CH_3NH_3PbI_3$/spiro-OMeTAD/graphite). Similar *J–V* hysteresis was observed for spiro-OMeTAD-based devices irrespective of whether a gold or graphite counter-electrode was used (Figures S6 and S7, Supporting Information). This result also indicates that the *J–V* hysteresis in not

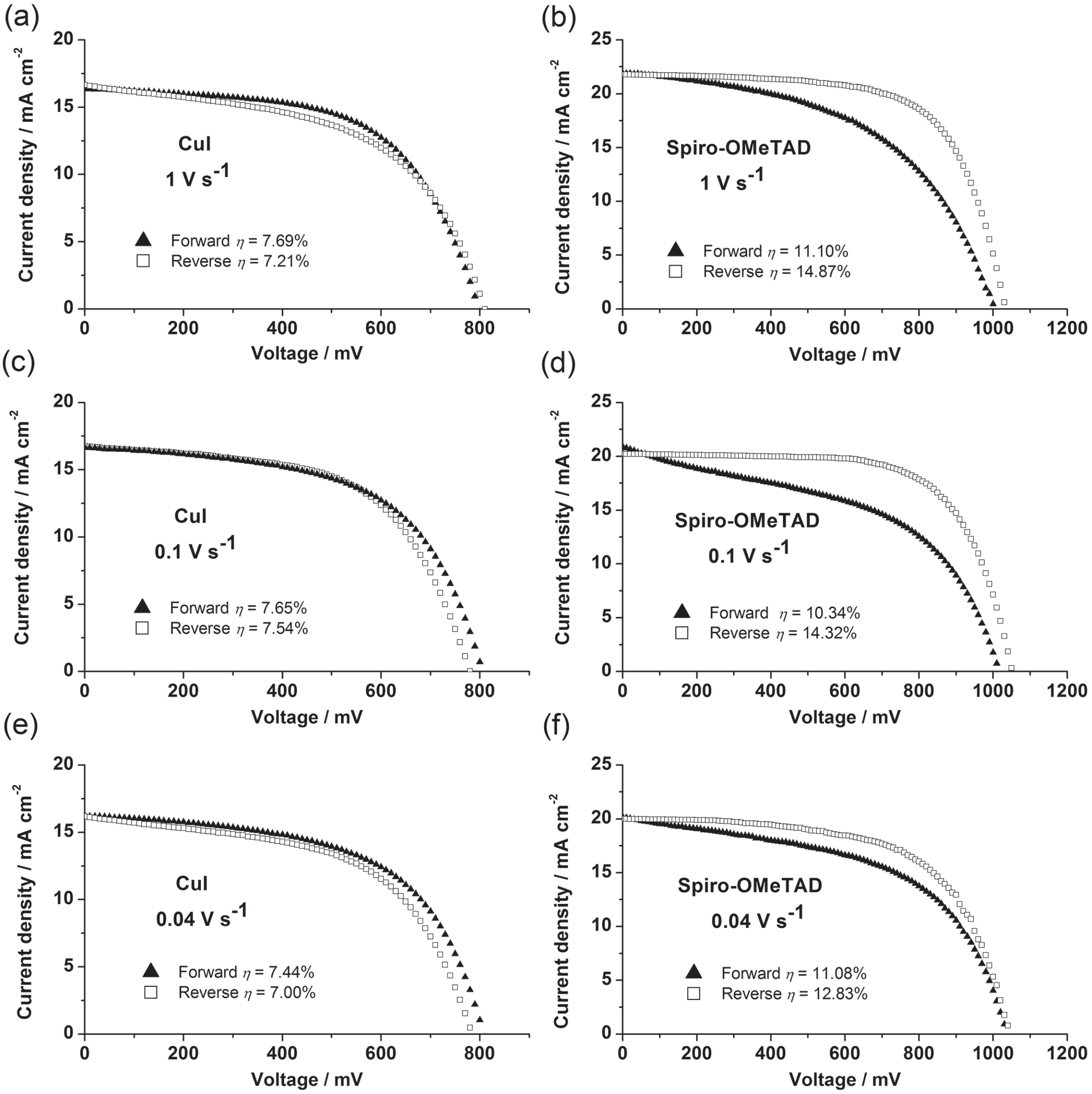

Figure 4. J–V curves of the CuI-based device at scan rates of a) 1 V s^{-1}; c) 0.1 V s^{-1}; and e) 0.04 V s^{-1}. J–V curves of a spiro-OMeTAD-based device at scan rates of b) 1 V s^{-1}; d) 0.1 V s^{-1}; and e) 0.04 V s^{-1}. Reverse ($V_{oc} \rightarrow V_0$) and forward ($V_0 \rightarrow V_{oc}$) scanning directions are shown for each scan rate. Each scan was performed independently to reduce any polarization (memory) effect remaining from previous scan. There was a dark interval of 30 s between each scan.

influenced by the lower performance of the CuI/graphite device (5.8 ± 0.8% average PCE) compared to the spiro-OMeTAD/graphite device (5.5 ± 2.1% average PCE), but more so by the different interfacial effects of the perovskite in contact with the CuI and spiro-OMeTAD materials.

2.2.5. Photoluminescence Quenching

Although the donor/acceptor interface is very important in terms of the exciton separation and assoiated PL quenching in organic photovoltaic systems, the low-exciton binding energy (only a few meV) in the perovskite phase allows spontaneous generation of free charge carriers upon photoexcitation under the ambient laboratory temperatures used in the present work.[28–30] The PL emission from the perovskite phase is a result of band-to-band radiative recombination of these free charge carriers. The use of a contacting HTM results in the quenching of PL from the perovskite film. Analysis of the PL quenching behavior of these systems provides information about the rate of the charge (hole) injection into the HTM material from the perovskite layer relative to that of recombination of photoinduced charges created within the perovskite phase.Therefore, PL emission measurements were performed on planar perovskite films, perovskite/spiro-OMeTAD bilayers, and perovskite/CuI bilayers (**Figure 6**a) formed directly on plain glass substrates to ascertain the efficiency of charge separation by the two hole conductors. The relative PL quenching by a contacting CuI layer is markedly greater than that of a spiro-OMeTAD layer. Similarly, the time-resolved PL

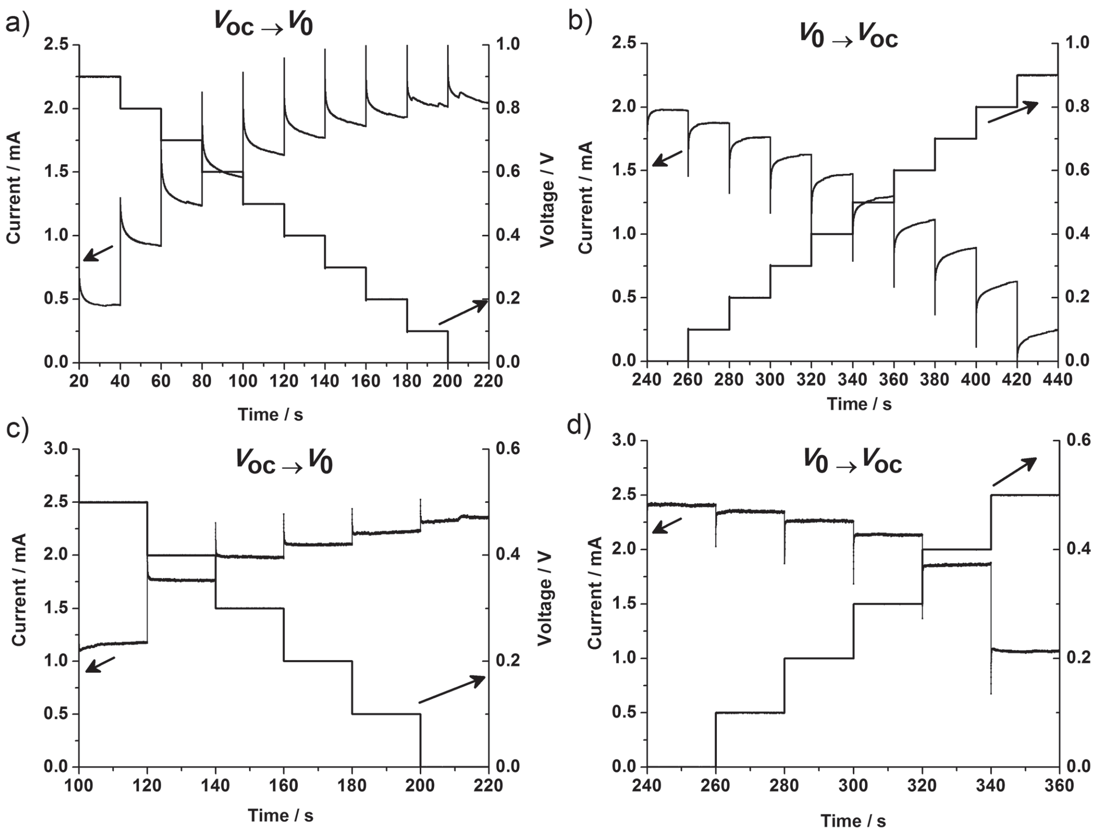

Figure 5. Steady-state current measurements using forward and reverse stepwise voltage sweeps for the spiro-OMeTAD-based (a, b) and CuI-based (c, d) devices.

decay data show that perovskite/CuI sample produces a faster decay compared to the perovskite/spiro-OMeTAD sample (Figure 6b). This is attributed to a more rapid injection of holes into the CuI layer, preventing the radiative recombination of carriers within the perovskite film. The PL results and *J–V* hysteresis observation cannot be directly related because the timescales of these two processes differ by several orders of magnitude.

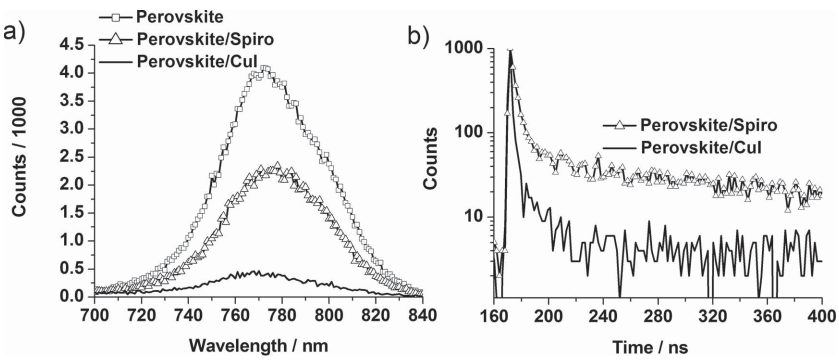

Figure 6. Photoluminescence emission spectrum of: a) perovskite film, perovskite/CuI bilayer and perovskite/spiro-OMeTAD bilayer systems; b) PL emission decay at 775 nm of perovskite/spiro-OMeTAD and perovskite/CuI bilayer systems. The films were coated on glass and illuminated from glass side.

2.2.6. Electrochemical Impedance Spectroscopy

EIS measurements can provide insights about charge transport, recombination, and accumulation of charges within the perovskite-based devices. Previously reported impedance studies of mesoscopic and planar structures typically observed two or three impedance features, including observations of a transmission-line response within both the mesoporous scaffold and the perovskite film itself.[67–70] However, subsequent reports of EIS in planar perovskite devices indicated that the observation of a transmission-line response, due to charge transport and recombination within the perovskite layer, is highly unlikely.[70] We have previously proposed an equivalent-circuit model, expanding on other formative studies,[71] to assign the two impedance features seen in planar perovskite devices.[72] The high-frequency feature is attributed largely to charge accumulation at the interface between the perovskite layer and the hole-selective or electron-selective materials[50,67,73] whereas the lower-frequency feature is suggested to be associated with the dielectric response of the perovskite layer[52,71] and the slow structural changes associated with this dielectric response.[74] Whether this characteristically slow response

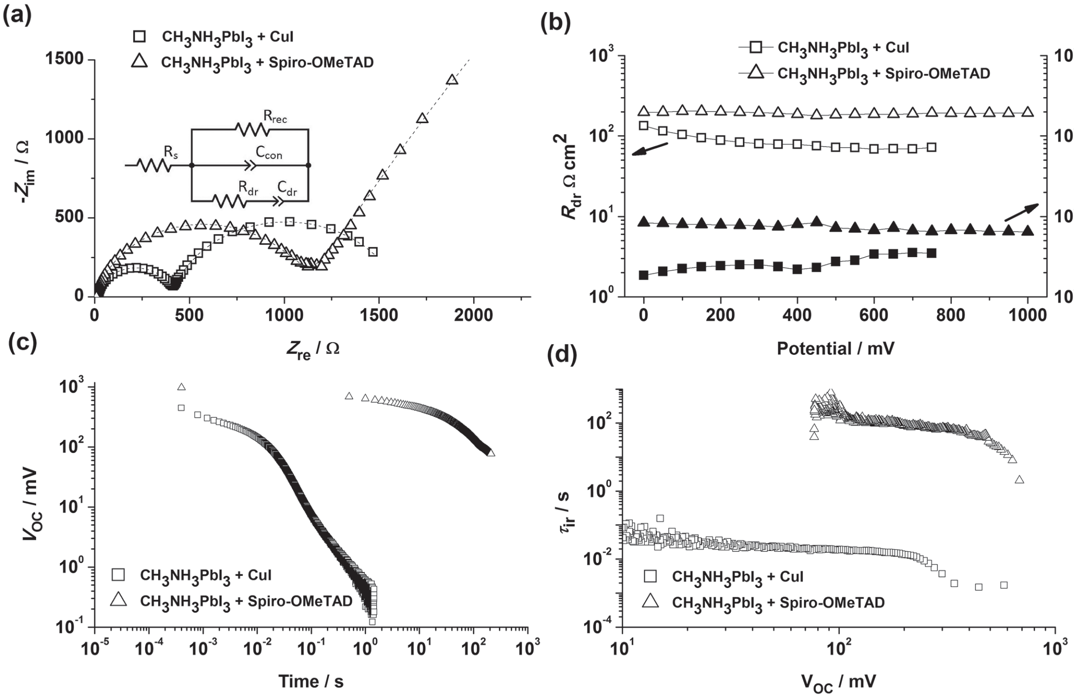

Figure 7. a) Nyquist plots obtained for a CuI-based device (circles) and a spiro-OMeTAD-based device (squares). Fits are shown in the dashed lines and the equivalence circuit used for fitting the impedance response is provided in the inset. b) Variation in R_{dr} and C_{dr} as a function of potential for both devices. Impedance measurements were performed under constant illumination. c) OCVD measurements for CuI-based and spiro-OMeTAD-based devices; and d) their corresponding instantaneous relaxation time constants, τ_{ir}, as a function of the V_{oc}.

is due to the dielectric polarization of the perovskite material,[52] or the movement of ions[54] is yet to be shown conclusively. The equivalent-circuit used to describe these two features comprises the series resistance, R_s, the interfacial recombination resistance, R_{rec}, the selective contact capacitance, C_{con}, the dielectric relaxation resistance, R_{dr}, and the dielectric contact capacitance, C_{dr} (**Figure 7**a). The equivalent-circuit elements describing the dielectric impedance response, R_{dr} and C_{dr}, are based on the widely used Debye relaxation model.[75] The R_{dr} and C_{dr} values calculated from the low-frequency feature reflect the dielectric polarization of the perovskite material. The slow dielectric response of the perovskite material, which is given by the low-frequency feature of EIS, has been cited as a possible source of the anomalous hysteresis seen in perovskite solar cells.[49]

The Nyquist plots shown in Figure 7a illustrate the high-frequency and low-frequency impedance features typically observed in planar perovskite solar cells.[70,72] The low-frequency intercept of the Z_{re} axis provides an indication of the interfacial recombination resistance, R_{rec}.[71] The curves in Figure 7a suggest that the interfacial recombination resistance in the CuI system is significantly lower than that of the spiro-OMeTAD system. This can be attributed to the relatively fast recombination rate at the perovskite/CuI interface, which was also observed by Christians et al.[41] The faster interfacial recombination in the CuI-based system was equally observed through photovoltage transients, as shown in Figure S5 (Supporting Information). Figure 7b shows the fitted R_{dr} and C_{dr} values for both the CuI-based and spiro-OMeTAD-based devices. The latter device type displays a higher dielectric relaxation resistance as well as a higher dielectric relaxation capacitance than the CuI-based device. As has been mentioned previously, these two equivalent-circuit parameters relate to the dielectric polarization of the perovskite material in the interfacial regions.[72] The higher C_{dr} and R_{dr} values in the spiro-OMeTAD-based device imply that there is both a stronger polarization of the perovskite material, and that this polarization is more resistant to relaxation.

In the case of the CuI-based devices, it is likely that the relatively fast charge recombination at the perovskite/CuI interface results in a smaller charge build-up, and a lower ensuing electric field at this interface. The electric field-induced response of the perovskite has been cited as a prominent factor affecting this slow behavior,[76] and it is likely that this response is most apparent at the high-field strength interfacial regions.[77] The weaker electric field experienced at the perovskite/CuI interface region may account for the reduced polarization of the perovskite dipoles in this interfacial region as seen in EIS results. Previous reports have discussed the effects of ion accumulation at the perovskite/contact interfaces and how this accumulation influences the slow response of perovskite solar cells.[55,78] The introduction of lithium salts into the spiro-OMeTAD material serves as an additional source of positive ions present at the perovskite/HTM interface. We postulate that excess positive charges present at this interface may be balanced by the polarization of the perovskite material. In the case of the perovskite/CuI interface, the number of balanced positive and negative charges is proposed to be significantly lower than at perovskite/spiro-OMeTAD interface. In this regard, perturbations to the quasi-Fermi level produce a faster response in the CuI-based devices. This effect can be further studied through transient techniques, such as photo-voltage decay.

2.2.7. Open-Circuit Voltage Decay

OCVD measurements were performed by illuminating a device at open circuit and then monitoring the decay of the voltage as carriers recombine after the illumination is switched off.[79] OCVD studies have been recognized as a simple and fast technique to determine recombination lifetime (τ_n) and have been used to investigate DSSCs.[79] Given that the open-circuit potential is governed by the separation of electron and hole quasi-Fermi levels within the perovskite layer, OCVD measurements provide valuable information concerning the density of charges remaining in the device. Therefore, OCVD measurements may reflect the polarization of the perovskite material and the trapping of charges at the perovskite/contacts interfaces. There have been some reports of OCVD measurements for perovskite solar cells describing two distinct stages in the decay;[52,80] a rapid decay in the millisecond timescale followed by a slow decay in 10–100 s scale.[80] The faster decay (Figure S5, Supporting Information) of $V_{\rm oc}$ has been attributed to the recombination of free charge carriers[81] and the slower decay (Figure 7c,d) to the relaxation of electric dipoles in perovskite film.[52] An instantaneous relaxation time, $\tau_{\rm ir}$, can be used to quantify the slow component of the OCVD response. In this work, we have used non-ideal relaxation, i.e., a function of voltage, which is determined through the following equation.[80]

$$\tau_{\rm ir}(V) \approx \left(-\frac{1}{V}\frac{\mathrm{d}V}{\mathrm{d}t}\right)^{-1} \tag{1}$$

Figure 7c depicts the slow component of the OCVD decay for both CuI-based and spiro-OMeTAD-based devices. The decay is significantly faster when CuI is employed as the HTM compared to spiro-OMeTAD (Figure 7c). The magnitude of $\tau_{\rm ir}$ as a function of the voltage reveals a significantly shorter relaxation time constant for the CuI-based device, which is several orders of magnitude smaller than for the spiro-OMeTAD-based device (Figure 7d).

The OCVD and EIS measurements indicate that the slow decay process is much slower in the spiro-OMeTAD-based device than in the CuI-based device. This comparatively slower response supports our postulate that the strong accumulation of positive charges in the spiro-OMeTAD layer is counterbalanced by the polarization of the interfacial perovskite layer. The sustained separation of these charges after the illumination is switched off leads to the slow OCVD response seen in the spiro-OMeTAD system. The CuI system, however, is unable to sustain this charge separation due to its lower interfacial capacitance and faster recombination dynamics.

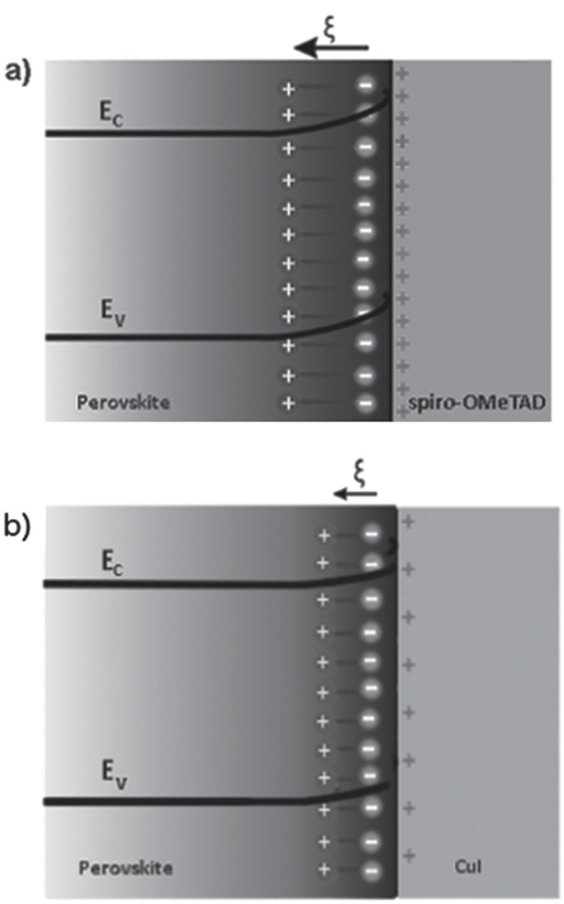

Figure 8. Schematic diagrams showing the strong dipoles and electric field produced at the a) perovskite/spiro-OMeTAD interface compared to weak field and dipoles at b) perovskite/CuI interface.

The schematic diagram in **Figure 8** depicts the relative electric-field gradient (the dark blue area shown in the perovskite phase) in the presence of different HTMs. Stronger polarization occurs at the perovskite/spiro-OMeTAD interface and weaker polarization at perovskite/CuI interface (relative strength of polarization shown by the distance between the positive and negative charges). The origin of this polarization is still in question as mentioned above. In both the EIS and OCVD measurements, the extremely slow response that is characteristic to spiro-OMeTAD-based devices was not observed for the CuI-based devices and cells incorporating a CuI HTM equally displayed little or no hysteresis in J–V measurements. We anticipate that relaxation of the polarization at the perovskite/HTM interface contributes to the hysteretic effect in the current–voltage response.

The perovskite/HTM interface therefore determines the relative extent of interfacial charge accumulation and the resulting electric-field strength and, consequently, the characteristically slow response of the device. In addition to the dielectric response of the perovskite material factors such as, for example, mobile ions[55,76] or trap-state discharging[49] could also be contributing to the J–V hysteresis. However, even if the dielectric response, as measured through EIS and OCVD transients, is not the only responsible factor, it is likely to contribute significantly to the observed J–V hysteresis phenomenon.

3. Conclusion

Thin films of methylammonium lead iodide perovskite as the photoactive layer and CuI as an inorganic HTM were deposited by rapid solution-based processes and used in the assembly of a planar-structured perovskite solar cell. The planar-structured devices exhibit a higher $V_{\rm oc}$ and $J_{\rm sc}$ than previously reported meso-structured perovskite/CuI solar cells. Moreover, this architecture resulted in a maximum PCE of 7.5% (average PCE of 5.8 ± 0.8%) for CuI-based devices with significantly diminished *J–V* hysteretic behavior in comparison to spiro-OMeTAD-based devices. It was demonstrated, using PL quenching data, that hole extraction at the perovskite/CuI interface is faster than at the perovskite/spiro-OMeTAD interface. Faster polarization relaxation was observed using EIS and OCVD for the perovskite/CuI system compared with the perovskite/spiro-OMeTAD system. We postulate that the magnitude of the charge separation is smaller at the perovskite/CuI interface compared to the perovskite/spiro-OMeTAD interface. This would lead to a smaller local electric field generated in the perovskite/CuI system compared to perovskite/spiro-OMeTAD system and, consequently, less polarization in the perovskite layer. Thus, the diminished hysteresis in *J–V* measurements of planar CuI-based devices is attributed mainly to the fast polarization relaxation.

4. Experimental Section

Materials: Most chemicals were purchased from Alfa Aesar (lead iodide) or Sigma–Aldrich (methylamine solution, hydriodic acid solution, *t*-BP, di-*n* -propylsulfide (Pr_2S), lithium bis(trifluoromethanesulfonyl) imide (LiTFSI), graphite powder <20 µm) and used as received. Spiro-OMeTAD was purchased from Luminescence Technology Corporation. FTO glass (3.2 mm thick, 8 Ω sq^{-1} sheet resistance) was purchased from Dyesol. CH_3NH_3I was synthesized by mixing solutions of CH_3NH_2 (20 mL, 0.23 mol, 40 wt% in water) and HI (10 mL, 76 mmol, 57 wt% in water) in water (100 mL). After stirring for 1 h, all volatiles were removed on a rotary evaporator at 60 °C. The product was dried in high vacuum (10^{-5} bar) at 60 °C for 24 h. The graphite suspension used for counter electrode fabrication was prepared by dispersing graphite particles (20 µm) in chlorobenzene (10 wt%) and ball milling for 4 h.

Dense TiO_2 Layer Fabrication: FTO-coated glass was laser engraved to separate the two electrodes and cleaned by ultra-sonication in 1% Helmanex surfactant solution, water, and ethanol, respectively. After drying, a dense TiO_2 layer was deposited onto the FTO substrate by spray pyrolysis of a $Ti(acac)_2(^iPrO)_2$ (bis(isopropoxide)bis(acetylacetonato) titanium(IV)) solution (1:9 $Ti(acac)_2(^iPrO)_2$:ethanol) at 450 °C.[82] Approximately 4 mL of this solution was sprayed on to the 10 × 10 cm substrate.

Perovskite Deposition: Various $(CH_3NH_3)PbI_3$ perovskite compositions between 40 and 50 wt% were used in optimization of the device performance (Figure S1, Supporting Information). For example, to prepare the 45% $(CH_3NH_3)PbI_3$ perovskite solution, stoichiometric amounts of lead iodide (PbI_2) (289 mg, 0.627 mmol) and methylammonium iodide (CH_3NH_3I) (99.7 mg, 0.627 mmol) were dissolved in dimethylformamide (500 µL), and the solution was stirred for 10 min. Other solutions were prepared by the same method. The perovskite solution (25 µL) was spin coated at 6500 rpm onto a substrate with an approximate area of 1 cm^2 using a gas-assisted deposition process.[53] Subsequently, the film was annealed at 100 °C on a hotplate for 10 min. The deposition and annealing were performed in a dry box under a nitrogen atmosphere.

CuI Deposition: CuI was deposited on the $(CH_3NH_3)PbI_3$ film in air by rapid doctor blading of a 0.1 M CuI solution (1:39 mixture of Pr_2 S/chlorobenzene) following the procedure of Christians et al.[41] Two drops of CuI solution were first placed on the edge of the glass substrate, which was maintained at 70 °C, and were allowed to heat for 30 s. The drawdown bar was then moved back and forth rapidly (approximately 5 cm s^{-1}) over the surface of the perovskite film until a thin layer of solution remained on the surface (Figure 1a). Once the solvent had evaporated, the process was repeated until four coating cycles were completed. The film was then left to dry on the hot plate at 70 °C for 1 min.

Spiro-OMeTAD Deposition: A spiro-OMeTAD solution was prepared by dissolving spiro-OMeTAD (20.8 mg, 17.0 mmol), LiTFSI (3.9 µL, 6.8 µmol of a 500 mg mL^{-1} stock solution in acetonitrile) and *t*-BP (8.4 µL, 57 µmol) in chlorobenzene (250 µL). A 25 µL aliquot of this solution was coated on the perovskite film by spin-coating at 3000 rpm for 30 s.

Counter-Electrode Fabrication: To complete the devices, two types of counter electrodes were used as follows (Figure 1b,c):

Type A (Gold): An elemental gold layer (100 nm) evaporated on the HTM layer using a thermal evaporator.

Type B (Graphite): For CuI-based devices, graphite particles (10–20 µm) were dispersed in chlorobenzene (10 wt%) and doctor bladed onto the CuI HTM layer and heated at 70 °C for 3 min. A Cu adhesive tape was placed on the graphite and a small pressure applied by hand with a Scotch adhesive tape in order to fix the Cu plate to the cell. The cathode cable was then soldered to Cu tape to complete the devices.

For the spiro-OMeTAD-based devices, the dispersion of graphite in chlorobenzene was doctor bladed on to poly(ethyleneterephthalate) film and dried in air. The graphite pad was then placed on the spiro-OMeTAD layer and pressed at 20 kpsi by cold isostatic pressing. The cathode cable was soldered to the substrate as it is in contact with graphite.

J–V Characterization: The *J–V* characteristics of the devices were recorded using a Keithley 2400 Source Meter. The device was illuminated using a xenon lamp source (100 mW cm^{-2}) provided by an Oriel solar simulator with an AM1.5 filter. A non-reflective mask with an aperture of 0.16 cm^2 was used to keep the irradiation area constant. The *J–V* scans were conducted at 10 mV steps with settling times of 10 ms (1 V s^{-1}), 100 ms (0.1 V s^{-1}), and 250 ms (0.04 V s^{-1}) in reverse ($V_{oc} \rightarrow V_0$) and forward ($V_0 \rightarrow V_{oc}$) directions. For the stepwise steady-state measurements, a bias was applied in 0.1 V increments until the V_{oc} of the device was reached. The current was measured at 0.01 s intervals for 20 s. Scanning was done in both $V_{oc} \rightarrow V_0$ and $V_0 \rightarrow V_{oc}$ directions. IPCE spectra were recorded using a Keithley 2400 Source Meter under 300 W xenon lamp irradiation with an Oriel Corner-stone 260 ¼ m monochromator.

Scanning Electron Microscopy Imaging: SEM images of the film surface and cross-sections of the perovskite solar cells were recorded on a FEI Nova NanoSEM 450 FEG microscope using a 5 kV acceleration voltage. The devices were prepared using the methods described above but without a counter electrode. For the cross-sectional images, devices were cut on the backside using a diamond glasscutter and broken in two.

Photoluminescence Measurements: PL measurements were performed using an Edinburgh Instruments Ltd. FLSP920 time-correlated single-photon counting (TCSPC) spectrometer. Steady-state measurements used a xenon lamp illumination source, while time-resolved measurements used a 465.8 nm pulsed diode laser excitation source (EPL-475, Edinburgh Instruments Ltd.) having a ≈100 ps pulse width and a peak laser excitation density of ≈0.2 nJ cm^{-2}. The luminescence was collected using a grating monochromator. Three types of samples were prepared on glass microscope slides with film areas of approximately 1 cm^2: (i) perovskite film; (ii) perovskite film with CuI deposited on top; and (iii) perovskite film with spiro-OMeTAD deposited on top.

Electrochemical Impedance Spectroscopy: The devices were illuminated using a 435 nm LED powered by a PP210 potentiostat. The EIS data were recorded using a 10 mV perturbation with varying applied potentials ranging from 0 V to the V_{oc}, performed in 0.05 V increments. A Zahner Zennium electrochemical workstation ECW IM6 was used as a frequency response analyzer, and impedance measurements were performed in the 4 MHz to 50 mHz frequency range. Impedance data were analyzed using Zview equivalent circuit modeling software (Scribner). Complete devices based on spiro-OMeTAD together with gold electrode and devices based on CuI together with graphite electrode were used to carry out the EIS measurements.

Open-Circuit Voltage Decay: Devices were illuminated with a 630 nm LED source with a switch-off response time of ≈20 µs. Voltage transients measured using NI-DAQMX USB-6212 data acquisition card. Complete devices based on spiro-OMeTAD together with gold electrode and devices based on CuI together with graphite electrode were used to carry out OCVD measurements.

Supporting Information

Supporting Information is available from the Wiley Online Library or from the author.

Acknowledgements

The authors acknowledge the Australian Centre for Advanced Photovoltaics, the Australian Renewable Energy Agency, and the Victorian State Government (DBI-VSA and DPI-ETIS) for financial support. Electron microscopy access provided by the Monash University Centre for Electron Microscopy (MCEM) is greatly acknowledged. The Alexander von Humboldt Foundation is gratefully acknowledged for a Feodor Lynen Fellowship to S.M. The Commonwealth Scientific and Industrial Research Organization is acknowledged for providing support through OCE Science Leader positions (U.B.).

Received: June 22, 2015
Revised: July 14, 2015

---

[1] A. Kojima, K. Teshima, Y. Shirai, T. Miyasaka, *J. Am. Chem. Soc.* **2009**, *131*, 6050.
[2] H. J. Snaith, *J. Phys. Chem. Lett.* **2013**, *4*, 3623.
[3] N.-G. Park, *J. Phys. Chem. Lett.* **2013**, *4*, 2423.
[4] H. Zhou, Q. Chen, G. Li, S. Luo, T.-B. Song, H.-S. Duan, J. Y. Z. Hong, Y. Liu, Y. Yang, *Science* **2014**, *345*, 542.
[5] M. K. Nazeeruddin, P. Gao, M. Gratzel, *Energy Environ. Sci.* **2014**, *7*, 2448.
[6] M. A. Green, A. Ho-Baillie, H. J. Snaith, *Nat. Photonics* **2014**, *8*, 506.
[7] W. S. Yang, J. H. Noh, N. J. Jeon, Y. C. Kim, S. Ryu, J. Seo, S. I. Seok, *Science* **2015**, *348*, 6240, 1234.
[8] J. Burschka, N. Pellet, S.-J. Moon, R. Humphry-Baker, P. Gao, M. K. Nazeeruddin, M. Gratzel, *Nature* **2013**, *499*, 316.
[9] M. He, D. Zheng, M. Wang, C. Lin, Z. Lin, *J. Mater. Chem. A* **2014**, *2*, 5994.
[10] M. Liu, M. B. Johnston, H. J. Snaith, *Nature* **2013**, *501*, 395.
[11] T. M. Koh, K. Fu, Y. Fang, S. Chen, T. C. Sum, N. Mathews, S. G. Mhaisalkar, P. P. Boix, T. Baikie, *J. Phys. Chem. C* **2014**, *118*, 16458.
[12] G. E. Eperon, S. D. Stranks, C. Menelaou, M. B. Johnston, L. M. Herz, H. J. Snaith, *Energy Environ. Sci.* **2014**, *7*, 982.
[13] W.-J. Yin, J.-H. Yang, J. Kang, Y. Yan, S.-H. Wei, *J. Mater. Chem. A* **2015**, *3*, 8926.
[14] N.-G. Park, *Mater. Today* **2015**, *18*, 65.
[15] O. Malinkiewicz, A. Yella, Y. H. Lee, G. M. Espallargas, M. Graetzel, M. K. Nazeeruddin, H. J. Bolink, *Nat. Photonics* **2014**, *8*, 128.
[16] J. H. Heo, S. H. Im, J. H. Noh, T. N. Mandal, C.-S. Lim, J. A. Chang, Y. H. Lee, H.-J. Kim, A. Sarkar, M. K. Nazeeruddin, M. Gratzel, S. I. Seok, *Nat. Photonics* **2013**, *7*, 486.
[17] P. Docampo, J. M. Ball, M. Darwich, G. E. Eperon, H. J. Snaith, *Nat. Commun.* **2013**, *4*, 2761.
[18] D. Liu, T. L. Kelly, *Nat. Photonics* **2014**, *8*, 133.
[19] J.-Y. Jeng, K.-C. Chen, T.-Y. Chiang, P.-Y. Lin, T.-D. Tsai, Y.-C. Chang, T.-F. Guo, P. Chen, T.-C. Wen, Y.-J. Hsu, *Adv. Mater.* **2014**, *26*, 4107.
[20] J. You, Z. Hong, Y. Yang, Q. Chen, M. Cai, T.-B. Song, C.-C. Chen, S. Lu, Y. Liu, H. Zhou, Y. Yang, *ACS Nano* **2014**, *8*, 1674.
[21] W. Ke, G. Fang, J. Wan, H. Tao, Q. Liu, L. Xiong, P. Qin, J. Wang, H. Lei, G. Yang, M. Qin, X. Zhao, Y. Yan, *Nat. Commun.* **2015**, *6*, 6700.
[22] S. Sun, T. Salim, N. Mathews, M. Duchamp, C. Boothroyd, G. Xing, T. C. Sum, Y. M. Lam, *Energy Environ. Sci.* **2014**, *7*, 399.
[23] J. H. Heo, H. J. Han, D. Kim, T. K. Ahn, S. H. Im, *Energy Environ. Sci.* **2015**, *8*, 1602.
[24] J. H. Im, C. R. Lee, J. W. Lee, S. W. Park, N. G. Park, *Nanoscale* **2011**, *3*, 4088.
[25] H. S. Kim, C. R. Lee, J. H. Im, K. B. Lee, T. Moehl, A. Marchioro, S. J. Moon, R. Humphry-Baker, J. H. Yum, J. E. Moser, M. Grätzel, N. G. Park, *Sci. Rep.* **2012**, *2*, 591.
[26] B. Conings, L. Baeten, C. De Dobbelaere, J. D'Haen, J. Manca, H.-G. Boyen, *Adv. Mater.* **2014**, *26*, 2041.
[27] N. A. Anderson, T. Lian, *Annu. Rev. Phys. Chem.* **2005**, *56*, 491.
[28] Y. Yamada, T. Nakamura, M. Endo, A. Wakamiya, Y. Kanemitsu, *IEEE. J. Photovoltaics* **2015**, *5*, 401.
[29] A. Miyata, A. Mitioglu, P. Plochocka, O. Portugall, J. T.-W. Wang, S. D. Stranks, H. J. Snaith, R. J. Nicholas, *Nat. Phys.* **2015**, *11*, 582.
[30] Y. Yamada, T. Nakamura, M. Endo, A. Wakamiya, Y. Kanemitsu, *J. Am. Chem. Soc.* **2014**, *136*, 11610.
[31] K. Wojciechowski, S. D. Stranks, A. Abate, G. Sadoughi, A. Sadhanala, N. Kopidakis, G. Rumbles, C.-Z. Li, R. H. Friend, A. K. Y. Jen, H. J. Snaith, *ACS Nano* **2014**, *8*, 12701.
[32] H. J. Snaith, M. Grätzel, *Appl. Phys. Lett.* **2006**, *89*, 262114.
[33] J. Krüger, R. Plass, L. Cevey, M. Piccirelli, M. Grätzel, U. Bach, *Appl. Phys. Lett.* **2001**, *79*, 2085.
[34] J. E. Kroeze, N. Hirata, L. Schmidt-Mende, C. Orizu, S. D. Ogier, K. Carr, M. Grätzel, J. R. Durrant, *Adv. Funct. Mater.* **2006**, *16*, 1832.
[35] G. Niu, X. Guo, L. Wang, *J. Mater. Chem. A* **2015**, *3*, 8970.
[36] Y. Han, S. Meyer, Y. Dkhissi, K. Weber, J. M. Pringle, U. Bach, L. Spiccia, Y.-B. Cheng, *J. Mater. Chem. A* **2015**, *3*, 8139.
[37] Z. Yu, L. Sun, *Adv. Energy Mater.* **2015**, *5*, 1500213.
[38] W. Li, H. Dong, L. Wang, N. Li, X. Guo, J. Li, Y. Qiu, *J. Mater. Chem. A* **2014**, *2*, 13587.
[39] M. Jørgensen, K. Norrman, F. C. Krebs, *Sol. Energy Mater. Sol. Cells* **2008**, *92*, 686.
[40] P. Qin, S. Tanaka, S. Ito, N. Tetreault, K. Manabe, H. Nishino, M. K. Nazeeruddin, M. Grätzel, *Nat. Commun.* **2014**, *5*, 3834.
[41] J. A. Christians, R. C. M. Fung, P. V. Kamat, *J. Am. Chem. Soc.* **2013**, *136*, 758.
[42] W. A. Laban, L. Etgar, *Energy. Environ. Sci.* **2013**, *6*, 3249.
[43] A. Mei, X. Li, L. Liu, Z. Ku, T. Liu, Y. Rong, M. Xu, M. Hu, J. Chen, Y. Yang, M. Grätzel, H. Han, *Science* **2014**, *345*, 295.
[44] S. Chavhan, O. Miguel, H.-J. Grande, V. Gonzalez-Pedro, R. S. Sanchez, E. M. Barea, I. Mora-Sero, R. Tena-Zaera, *J. Mater. Chem. A* **2014**, *2*, 12754.
[45] S. Ito, S. Tanaka, H. Nishino, *J. Phys. Chem. Lett.* **2015**, *6*, 881.
[46] S. Ye, W. Sun, Y. Li, W. Yan, H. Peng, Z. Bian, Z. Liu, C. Huang, *Nano Lett.* **2015**, *15*, 3723.
[47] A. S. Subbiah, A. Halder, S. Ghosh, N. Mahuli, G. Hodes, S. K. Sarkar, *J. Phys. Chem. Lett.* **2014**, *5*, 1748.
[48] X. Xu, Z. Liu, Z. Zuo, M. Zhang, Z. Zhao, Y. Shen, H. Zhou, Q. Chen, Y. Yang, M. Wang, *Nano Lett.* **2015**, *15*, 2402.
[49] H. J. Snaith, A. Abate, J. M. Ball, G. E. Eperon, T. Leijtens, N. K. Noel, S. D. Stranks, J. T.-W. Wang, *J. Phys. Chem. Lett.* **2014**, *5*, 1511.
[50] A. Dualeh, T. Moehl, N. Tétreault, J. Teuscher, P. Gao, M. K. Nazeeruddin, M. Grätzel, *ACS Nano* **2013**, *8*, 362.
[51] H.-S. Kim, N.-G. Park, *J. Phys. Chem. Lett.* **2014**, *5*, 2927.
[52] R. S. Sanchez, V. Gonzalez-Pedro, J.-W. Lee, N.-G. Park, Y. S. Kang, I. Mora-Sero, J. Bisquert, *J. Phys. Chem. Lett.* **2014**, *5*, 2357.

[53] E. L. Unger, E. T. Hoke, C. D. Bailie, W. H. Nguyen, A. R. Bowring, T. Heumuller, M. G. Christoforo, M. D. McGehee, *Energy Environ. Sci.* **2014**, *7*, 3690.
[54] Z. Xiao, Y. Yuan, Y. Shao, Q. Wang, Q. Dong, C. Bi, P. Sharma, A. Gruverman, J. Huang, *Nat. Mater.* **2015**, *14*, 193.
[55] Y. Zhao, C. Liang, H. Zhang, D. Li, D. Tian, G. Li, X. Jing, W. Zhang, W. Xiao, Q. Liu, F. Zhang, Z. He, *Energy Environ. Sci.* **2015**, *8*, 1256.
[56] S. Inudo, M. Miyake, T. Hirato, *Phys. Status Solidi A* **2013**, *210*, 2395.
[57] P. Pattanasattayavong, G. O. N. Ndjawa, K. Zhao, K. W. Chou, N. Yaacobi-Gross, B. C. O'Regan, A. Amassian, T. D. Anthopoulos, *Chem. Commun.* **2013**, *49*, 4154.
[58] F. Huang, Y. Dkhissi, W. Huang, M. Xiao, I. Benesperi, S. Rubanov, Y. Zhu, X. Lin, L. Jiang, Y. Zhou, A. Gray-Weale, J. Etheridge, C. R. McNeill, R. A. Caruso, U. Bach, L. Spiccia, Y.-B. Cheng, *Nano Energy* **2014**, *10*, 10.
[59] W.-J. Yin, T. Shi, Y. Yan, *Adv. Mater.* **2014**, *26*, 4653.
[60] J. H. Noh, N. J. Jeon, Y. C. Choi, M. K. Nazeeruddin, M. Gratzel, S. I. Seok, *J. Mater. Chem. A* **2013**, *1*, 11842.
[61] E. Edri, S. Kirmayer, D. Cahen, G. Hodes, *J. Phys. Chem. Lett.* **2013**, *4*, 897.
[62] L. Etgar, P. Gao, Z. Xue, Q. Peng, A. K. Chandiran, B. Liu, M. K. Nazeeruddin, M. Grätzel, *J. Am. Chem. Soc.* **2012**, *134*, 17396.
[63] W. Tress, N. Marinova, O. Inganäs, M. K. Nazeeruddin, S. M. Zakeeruddin, M. Graetzel, *Adv. Energy Mater.* **2014**, *5*, 1400812.
[64] J. H. Noh, S. H. Im, J. H. Heo, T. N. Mandal, S. I. Seok, *Nano Lett.* **2013**, *13*, 1764.
[65] J. M. Frost, K. T. Butler, F. Brivio, C. H. Hendon, M. van Schilfgaarde, A. Walsh, *Nano Lett.* **2014**, *14*, 2584.
[66] E. J. Juarez-Perez, R. S. Sanchez, L. Badia, G. Garcia-Belmonte, Y. S. Kang, I. Mora-Sero, J. Bisquert, *J. Phys. Chem. Lett.* **2014**, *5*, 2390.
[67] E. J. Juarez-Perez, M. Wuβler, F. Fabregat-Santiago, K. Lakus-Wollny, E. Mankel, T. Mayer, W. Jaegermann, I. Mora-Sero, *J. Phys. Chem. Lett.* **2014**, *5*, 680.
[68] E. Guillén, F. J. Ramos, J. A. Anta, S. Ahmad, *J. Phys. Chem. C* **2014**, *118*, 22913.
[69] G. Xing, N. Mathews, S. Sun, S. S. Lim, Y. M. Lam, M. Grätzel, S. Mhaisalkar, T. C. Sum, *Science* **2013**, *342*, 344.
[70] A. Pockett, G. E. Eperon, T. Peltola, H. J. Snaith, A. B. Walker, L. M. Peter, P. J. Cameron, *J. Phys. Chem. C* **2015**, *119*, 3456.
[71] J. Bisquert, L. Bertoluzzi, I. Mora-Sero, G. Garcia-Belmonte, *J. Phys. Chem. C* **2014**, *118*, 18983.
[72] A. R. Pascoe, N. W. Duffy, A. D. Scully, F. Huang, Y.-B. Cheng, *J. Phys. Chem. C* **2015**, *119*, 4444.
[73] V. Gonzalez-Pedro, E. J. Juarez-Perez, W.-S. Arsyad, E. M. Barea, F. Fabregat-Santiago, I. Mora-Sero, J. Bisquert, *Nano Lett.* **2014**, *14*, 888.
[74] R. Gottesman, E. Haltzi, L. Gouda, S. Tirosh, Y. Bouhadana, A. Zaban, E. Mosconi, F. De Angelis, *J. Phy. Chem. Lett.* **2014**, *5*, 2662.
[75] A. K. Jonscher, *J. Phys. D: Appl. Phys.* **1999**, *32*, R57.
[76] W. Tress, N. Marinova, T. Moehl, S. M. Zakeeruddin, M. K. Nazeeruddin, M. Gratzel, *Energy Environ. Sci.* **2015**, *8*, 995.
[77] M. Zeman, J. A. Willemen, L. L. A. Vosteen, G. Tao, J. W. Metselaar, *Sol. Energy Mater. Sol. Cells* **1997**, *46*, 81.
[78] O. Almora, I. Zarazua, E. Mas-Marza, I. Mora-Sero, J. Bisquert, G. Garcia-Belmonte, *J. Phys. Chem. Lett.* **2015**, *6*, 1645.
[79] A. Zaban, M. Greenshtein, J. Bisquert, *ChemPhysChem* **2003**, *4*, 859.
[80] L. Bertoluzzi, R. S. Sanchez, L. Liu, J.-W. Lee, E. Mas-Marza, H. Han, N.-G. Park, I. Mora-Sero, J. Bisquert, *Energy Environ. Sci.* **2015**, *8*, 910.
[81] A. Baumann, K. Tvingstedt, M. C. Heiber, S. Väth, C. Momblona, H. J. Bolink, V. Dyakonov, *APL Mater.* **2014**, *2*, 081501.
[82] L. Kavan, M. Grätzel, *Electrochim. Acta* **1995**, *40*, 643.